J. Fluid Mech. (2026), *vol.* 1037, A11, doi:10.1017/jfm.2026.11586

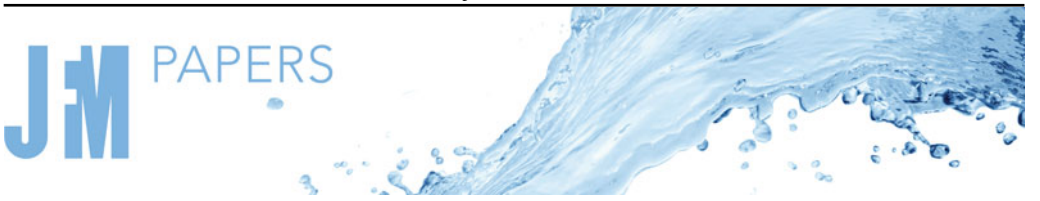

Fast droplet impact onto slowly moving deep pools

Thomas C. Sykes[1,2], **Luke Alventosa**[3], **J. Rafael Castrejón-Pita**[4], **Radu Cimpeanu**[5], **Daniel M. Harris**[3] and **Alfonso A. Castrejón-Pita**[2]

[1]School of Engineering, University of Warwick, Coventry CV4 7AL, UK

[2]Department of Engineering Science, University of Oxford, Oxford OX1 3PJ, UK

[3]School of Engineering, Brown University, Providence, RI 02912, USA

[4]Department of Mechanical Engineering, University College London, London WC1E 7JE, UK

[5]Mathematics Institute, University of Warwick, Coventry CV4 7AL, UK

Corresponding author: Thomas C. Sykes, thomas.sykes@warwick.ac.uk

(Received 4 November 2025 UTC; revised 19 March 2026 UTC; accepted 21 April 2026 UTC)

When a fast droplet impacts a pool, the resulting ejecta sheet dynamics determine the final impact outcome. At low capillary numbers, the ejecta sheet remains separate from a deep static pool, while at higher values, it develops into a lamella. Here, we show that the common natural scenario of a slowly moving deep pool can change the upstream impact outcome, creating highly three-dimensional dynamics no longer characterised by a single descriptor. By considering how pool movement constrains the evolution of the ejecta sheet angle, we reach a length-scale invariant parametrisation for the upstream transition that holds for a wide range of fluids and impact conditions. Direct numerical simulations show similar dynamics for an equivalent oblique impact, indicating that the air boundary layer above a moving pool does not play a decisive role for low pool–droplet speed ratios. Our results also provide insight into the physical mechanisms that underpin pool impact outcomes more generally.

Key words: breakup/coalescence, drops, interfacial flows (free surface)

1. Introduction

Most droplet impact research concerns normal collisions with a static substrate. However, in many natural and industrial processes, droplets impact obliquely or onto a moving substrate. This seemingly subtle distinction transforms droplet impact from the typical

axisymmetric configuration to be inherently three-dimensional. Example processes include raindrops splashing on the moving ocean that contributes to air–sea exchange (Anguelova 2021), inkjet printing onto moving paper (Lohse 2022), and crop spraying with numerous droplet impacts at arbitrary angles (Gielen *et al.* 2017).

Most of the existing literature on moving substrates has considered dry surfaces, where horizontal surface motion can modify splashing thresholds (Bird, Tsai & Stone 2009; Hao & Green 2017), alter spreading factors (Li *et al.* 2024), and even generate new impact outcomes such as boundary-layer-driven 'aerodynamic rebound' (Stumpf *et al.* 2025). Likewise, inclined solid surfaces yield asymmetric crowns and reduce splashing propensity (Hao *et al.* 2019).

When the substrate is a pool, either moving or with a droplet impacting obliquely, the literature is more limited and exploratory. Castrejón-Pita *et al.* (2016) identified distinct regimes (including a new 'surfing' outcome) that depend on the pool–droplet speed ratio, but could not explore low pool speeds. Several studies have considered thin films that are either flowing (Guo *et al.* 2025) or obliquely impacted (Bao *et al.* 2025). A few authors have considered oblique impact (Gielen *et al.* 2017; Reijers *et al.* 2019), and moving (Gupta & Kumar 2020), deep pools. However, all of these works focused on long time scale dynamics such as crater evolution, crown structure and the Worthington jet.

For static pools, following the observation that high-speed droplet impact leads to the formation of an ejecta sheet (Weiss & Yarin 1999; Thoroddsen 2002), it is now well understood that the ejecta sheet dynamics on very short time scales determine impact outcomes (Wang *et al.* 2023). Using X-ray imaging, Zhang *et al.* (2012) confirmed that at low Reynolds numbers Re, a single sheet-like jet (termed a lamella) is formed by droplet impact on a deep pool. The lamella subsumes the ejecta sheet, which collects fluid from the pool as it develops. At higher Re, the ejecta sheet remains a separate structure and is later accompanied by a roll jet, using the nomenclature of Agbaglah *et al.* (2015). A variety of dynamics associated with the ejecta sheet in the latter regime are seen, including the protrusion, quartering, and irregular splashing outcomes identified by Thoraval *et al.* (2012). At high Re in the irregular splashing regime, Thoraval *et al.* (2012) predicted from numerical simulations that the base of the ejecta sheet would be unstable and produce a von Kármán vortex street, which was experimentally observed by Castrejón-Pita *et al.* (2012). Here, we use the term separate ejecta sheet (SES) as an umbrella term for all non-lamella outcomes, which is consistent with Zhang *et al.* (2012) and our previous work (Sykes *et al.* 2023). Agbaglah *et al.* (2015) showed that the development of the SES outcome is driven by vortex shedding; the transition between a lamella and SES is associated with a fixed capillary number $Ca = 0.2$. Here, we extend our knowledge of ejecta sheet behaviour to include pool movement, showing that impact outcomes can differ upstream and downstream only when $Ca < 0.2$. The transition can be explained by considering the evolution of the ejecta sheet angle, giving a length-scale invariant parametrisation of Ca and the square root of the pool–droplet velocity ratio.

2. Methods

2.1. *Experiments*

Millimetric droplets were dripped from a blunt-end dispensing tip and impacted normally onto a deep pool, both consisting of the same fluid: distilled water, five glycerol–water mixtures, and two silicone oils – see table 1, where fluid properties and absolute errors (used in propagation of error analyses) are tabulated. Six dispensing tips (15–30 gauge, outer diameters 0.31–1.83 mm) were used to modify the droplet diameter

Fluid (**short name**)	Density ρ (kg m^{-3})	Dynamic viscosity μ (mPa s)	Surface tension σ (mN m^{-1})
Distilled **water**	997 ± 1	0.93 ± 0.01	72.4 ± 0.2
21 vol% glycerol–water	1058 ± 1	1.9 ± 0.0	71.0 ± 0.3
32 vol% glycerol–water	1089 ± 1	3.0 ± 0.1	70.3 ± 0.2
43 vol% glycerol–water	1122 ± 1	5.4 ± 0.2	69.0 ± 0.4
47 vol% glycerol–water	1134 ± 2	6.5 ± 0.3	68.4 ± 0.5
51 vol% glycerol–water	1145 ± 2	8.0 ± 0.3	67.8 ± 0.4
1 cSt silicone oil	816	0.8	17.4
2 cSt silicone oil	870	1.7	18.7

Table 1. Fluid properties of the droplet and pool (same fluid). The density of each glycerol–water mixture (glycerol, Acros Organics 99 % pure) was measured using a 25 ml density bottle and 1 mg precision analytical balance, dynamic viscosity with a vibrational viscometer (Hydramotion Viscolite 700, 0.1 mPa s precision), and surface tension with a Sinterface BPA-2S tensiometer. Measured viscosities were confirmed to be consistent with known empirical correlations (Cheng 2008). Silicone oils (Clearco Products) were used as received; the fluid properties reported are those from the product data sheet. All values are reported for 23 ± 1 °C.

$D \in [2.20, 3.75]$ mm, which provides our characteristic length scale via the circle-fitted nominal radius r_n (see the supplementary material available at 10.1017/jfm.2026.11586.). The dispensing tip height relative to the pool free surface was varied (205–575 mm) to adjust the normal impact velocity, $u_n \in [1.6, 3.2]$ m s^{-1}. Absolute errors of ± 0.01 m for r_n and ± 0.01 m s^{-1} for u_n are assumed. The variation in u_n was primarily responsible for the range $We = \rho u_n^2 D/\sigma \in [134, 450]$, while the different fluids enabled considerable variation in $Re = \rho u_n D/\mu \in [940, 7930]$ (figure 1*a*). As the capillary number $Ca = We/Re = \mu u_n/\sigma$ proves influential, we non-dimensionalise times with the visco-capillary time scale $\mu D/\sigma$ (dimensionless times are denoted by t_μ^*).

For all experiments, the pool depth h was maintained such that $h/D > 3$ (typically with $h \in [12, 14]$ mm), which is sufficient that the pool can be considered deep for the early-time dynamics of interest here (Thoroddsen *et al.* 2011; Sykes *et al.* 2023). Pool movement was achieved using a belt-driven rotating table fitted with an optically clear annular tank (figure 1*b*) of outer diameter 588 mm (constructed from a 600 mm diameter cast acrylic tube with 6 mm wall thickness) and inner diameter 450 mm – see the supplementary material for further details. The inner walls were treated with a commercial hydrophobic coating (Rain-X Plastic Water Repellent) to curtail the formation of a meniscus that would interfere with side-view imaging. The experiments involving silicone oils used a similar set-up described in Harris *et al.* (2026). Using rotation to engender pool movement – as opposed to a simple linear translation of the pool – inevitably leads to a curved parabolic free surface in the direction orthogonal to the direction of pool movement, which is shown to be inconsequential for our results in § 3.6.

Practical limitations restricted the maximum rotational frequency to approximately 0.5 Hz, with linear pool speeds at the impact point of $u_t \in [0, 0.6]$ m s^{-1} reported here. The pool velocity u_t was calculated from the rotation rate of the table, which was determined by monitoring the time for each quarter-rotation using an optical switch (Optek OPB900W55Z) connected to a data logger (Moku:Go). The implied u_t therefore assumes that the fluid is in solid-body rotation with the tank, and that the effect of air drag on the free surface is negligible. The typical time scale associated with spin-up of a fluid in a (non-annular) cylinder, from rest to angular velocity Ω, is $t_E = Ek^{-1/2}\Omega^{-1} = h\sqrt{\rho/\mu\Omega}$, where $Ek = \mu/\Omega\rho h^2$ is the Ekman number (Greenspan & Howard 1963). This time scale applies even when the cylinder is partially filled, since the bottom-wall Ekman layer is primarily responsible for spin-up (Homicz & Gerber 1987), and is a factor of $Ek^{1/2}$ shorter

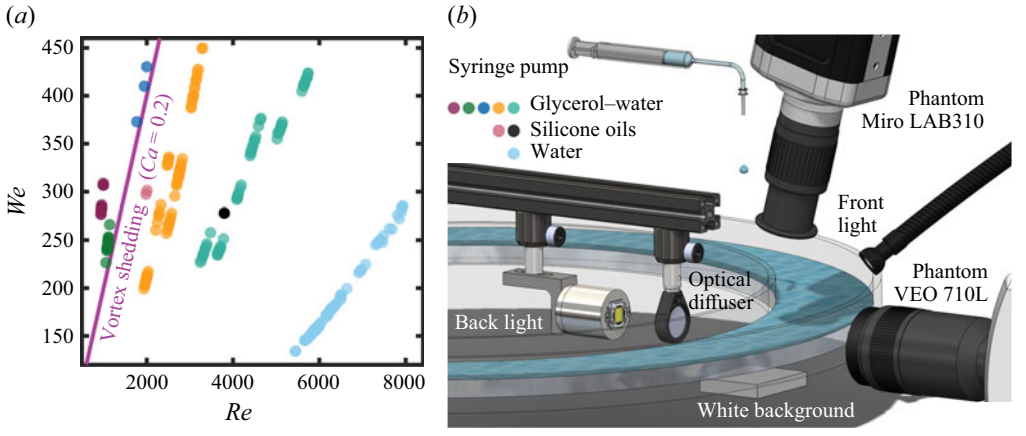

Figure 1. (*a*) Plots of *We* versus *Re* for all experiments reported. Error bars based on a propagation of error analysis (see § 2.1 for assumed absolute errors) would be smaller than each marker so are omitted. The purple line delineates the known vortex shedding boundary ($Re = 5\,We$, i.e. $Ca = 0.2$; Agbaglah *et al.* 2015). (*b*) A rendering of the experimental set-up.

than the viscous diffusion time scale due to the effect of Ekman suction. Here, $t_E \leq 40$ s, which suggests that the allowed spin-up time of approximately 5 min for all experiments was sufficient. Particle tracking velocimetry experiments were also used to verify the actual free surface speeds – see the supplementary material (Crocker & Grier 1996). An absolute error ± 0.02 m s^{-1} for u_t is assumed, which typically dominates our propagated uncertainties (e.g. in figure 4 below).

Impacts were imaged from the side (through the side wall of the tank, figure 1*b*) with a Phantom VEO 710L high-speed camera (7500–14 000 fps, 3–12 µs exposure) in a shadowgraphy configuration, using a Laowa 100 mm lens (64–89 pixels mm^{-1}). A second front-lit high-speed camera (Phantom Miro LAB310, colour sensor, 4800–6300 fps, 40–70 µs exposure), mounted 15° from vertical to keep the path of the falling droplet free, simultaneously imaged from an oblique viewpoint using a Tamron SP AF 90 mm lens (30–40 pixels mm^{-1}).

2.2. *Direct numerical simulation*

We constructed a high-fidelity computational counterpart of our system using the Basilisk open-source environment (Popinet 2009, 2015), which has been successfully used in recent years for supporting both experimental and theoretical high-speed droplet impact research to gain additional physical insight into rapidly evolving ejecta sheet dynamics (e.g. Fudge *et al.* 2023; Sykes *et al.* 2023). The computational box is three-dimensional, with a symmetry boundary condition used on the plane spanned by the pool and droplet velocity vectors (figure 2*a*). The domain measures $5r_n$ in each dimension, with either an imposed uniform unidirectional velocity field or outflow prescribed at the remaining boundaries. The pool occupies half of the domain in height, with the drop being initially placed with its south pole $0.1r_n$ above the surface. While embedded within the boundary layer of the moving pool (see § 3.6 for further discussion), we observe negligible changes (<0.1 %) in both trajectory and velocity prior to impact based on measurements of the centre of mass during the early stages of our simulations.

Employing adaptive mesh refinement based on interfacial position location and changes in magnitudes of the velocity components and the vorticity allows us to restrict the computational effort to $\mathcal{O}(10^7)$ computational grid cells while maintaining an $\mathcal{O}(1)$ µm

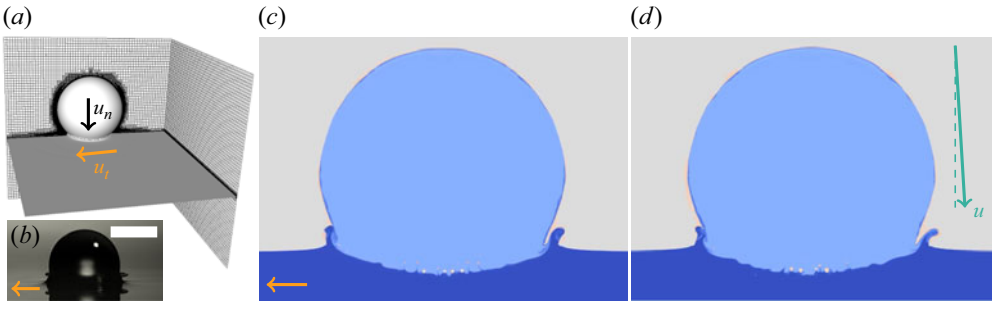

Figure 2. (*a*) Computational box highlighting adaptive grid refinement. (*b*) Experimental view of the case described by $Ca = 0.105$ (32 vol% fluid) and $u_t = 0.15$ m s^{-1} ($u_n = 2.45$ m s^{-1}, $\sqrt{u_t/u_n} = 0.25$), at $t^*_\mu = 2$. The upstream outcome is a lamella. The orange arrow indicates the direction of pool movement, and the scale bar is 2 mm. (*c*) The result of a simulation matching the conditions in (*b*) with tracer fields used to visualise liquid originating from the droplet and the pool separately. As in the experiment, a lamella is seen upstream. (*d*) An equivalent oblique impact ($u_o = \sqrt{u_t{}^2 + u_n^2} = 2.455$ m s^{-1}, $\beta = \tan^{-1}(u_t/u_n) = 3.5°$) on a static pool ($u_t = 0$ m s^{-1}). The droplet falls from left to right here, in the direction indicated by the green arrow (dashed is vertical). A lamella is seen on the leading side, which corresponds to upstream on a moving pool.

resolution level for the most resource-intensive flow regions, illustrated in figure 2(*a*). Lowering the maximum allowed dimensionless time step to $\Delta t = 10^{-3}$, and adjusting the multigrid solver specifications (higher number of iterations allowed to achieve convergence, defined with a lower target threshold to ensure high accuracy) for key stages of the flow, particularly during initial coalescence, are additional features incorporated in our implementation to ensure the robustness of our calculations. With these specifications, a typical run that represents approximately 0.5 ms in real time requires $\mathcal{O}(10^4)$ CPU hours to complete. A dedicated repository for the source code and typical parametric set-up is provided on GitHub. In § 3.6, we use these simulations to compare normal impact onto a moving pool with oblique impact onto a static pool, with the code and pre-processing scripts being set up to flexibly accommodate both scenarios.

3. Results and discussion

3.1. *Impact outcomes on moving $Ca < 0.2$ pools*

Initially, we consider $Ca < 0.2$ impacts, for which a static deep pool produces an SES outcome. Figure 3 shows a representative case ($Ca = 0.132$, 32 vol%) where only the pool speed $u_t \in \{0, 0.17, 0.26\}$ m s^{-1} is varied. As expected, a generally axisymmetric SES is seen for a static pool in figure 3(*a*). The ejecta sheet folding towards the axis of symmetry is clearly visible as an inner circle in the oblique view (bottom row), especially at $t^*_\mu = 5$. For $u_t = 0.17$ ms^{-1} (figure 3*b*), the dynamics are not axisymmetric, but an SES outcome is maintained in all directions. However, when the pool speed is increased further to $u_t = 0.26$ m s^{-1} (figure 3*c*), the ejecta sheet develops into a lamella upstream. This outcome is typically seen on viscous ($Ca > 0.2$) or shallow (Sykes *et al.* 2023) static pools. An SES is maintained downstream and in most directions (see the oblique view) except for ∼70° around the upstream side. That is, above a critical pool speed, the upstream impact outcome transitions from an SES to a lamella.

3.2. *Delineating the upstream transition boundary*

The capillary number is the appropriate quantity to represent droplet impact on deep pools (Agbaglah *et al.* 2015). To delineate the upstream transition, we also need to determine

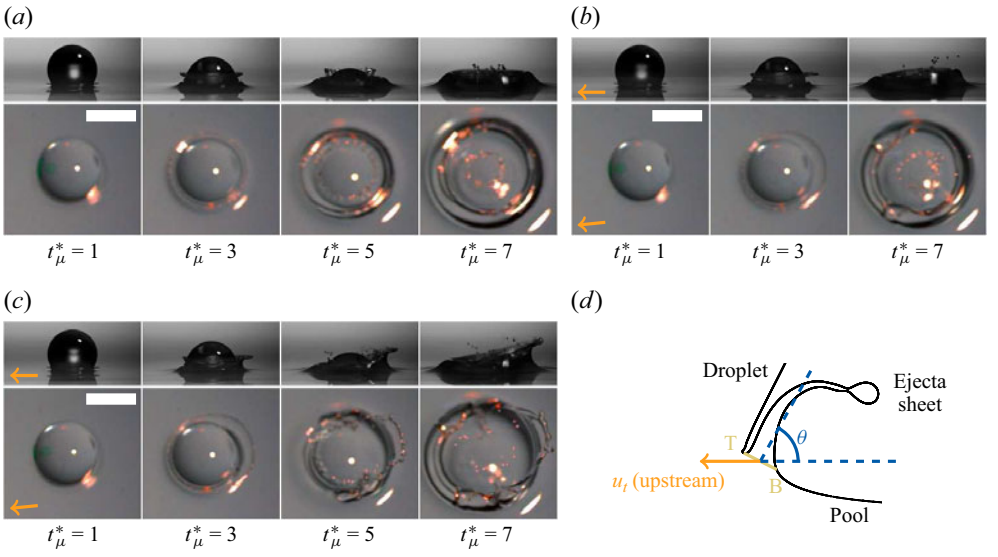

Figure 3. Typical ejecta sheet dynamics associated with pool movement, at a fixed capillary number. (*a–c*) Images for $Ca = 0.132$ ($We = 345$, $u_n = 3.10$ m s^{-1}) impact of a 32 vol% droplet onto a 32 vol% deep pool. Except for the satellite droplets, the bright spots visible in the oblique view images are artefacts of the front lighting used; they have a light orange appearance due to the use of a colour high-speed camera. (*a*) The pool is static: SES, which is expected since $Ca < 0.2$ (figure 1*a*). (*b*) The pool moves with $u_t = 0.17$ m s^{-1} ($\sqrt{u_t/u_n} = 0.23$): SES, but the ejecta sheet dynamics are not axisymmetric. (*c*) The pool moves with $u_t = 0.26$ m s^{-1} ($\sqrt{u_t/u_n} = 0.29$): lamella upstream and an SES downstream. (*d*) Sketch of an ejecta sheet, where points T and B are the maximum radii of curvature of the free surface on the droplet and pool, respectively. Together, they define the ejecta sheet base TB. The acute angle subtended between the normal to TB and the horizontal, θ, is the ejecta sheet angle, following the definition in Thoraval *et al.* (2012). Orange arrows indicate the direction of pool movement, and all scale bars are 2 mm.

a suitable dimensionless quantity to represent pool movement. Thoroddsen *et al.* (2011) developed a simple geometric model to describe ejecta sheet dynamics, in which the ejection velocity (for some time $t > 0$ at which the ejecta sheet begins to propagate outwards faster than the radial velocity of the contact point, 'out-running' the droplet) is directed tangentially to a sphere approximating the droplet, and is proportional in magnitude to $u_n \cos\theta$. Here, θ is the angle between the tangent to the sphere at the pool–droplet contact line and the horizontal, akin to the ejecta sheet angle (defined below). Geometrically, θ is also the angle subtended at the sphere/droplet centre by the droplet impact velocity vector (vertical in the case of normal impact) and the radial line to the pool–droplet contact line. In our work, the pre-impact droplet and pool velocity vectors are orthogonal; the resultant velocity vector is directed at an angle β from the vertical, where $\tan\beta = u_t/u_n \approx \beta$ since $u_t \ll u_n$. For a geometrically equivalent oblique impact at an angle β from the vertical on a static pool (discussed further in § 3.6), the 'leading side' (adopting the nomenclature of Reijers *et al.* 2019) is equivalent to upstream, which can be understood by considering that a normally impacting droplet would appear to be falling backwards by an observer travelling on a moving pool. Therefore, for a $\beta > 0$ oblique impact, θ is effectively reduced at the time of ejection, as the droplet impact velocity vector is no longer vertical, but rather pointed towards the leading side.

To determine how the ejecta sheet angle grows with time post-ejection, Thoraval *et al.* (2012) defined the ejecta sheet base as the line segment (yellow line in figure 3*d*) between

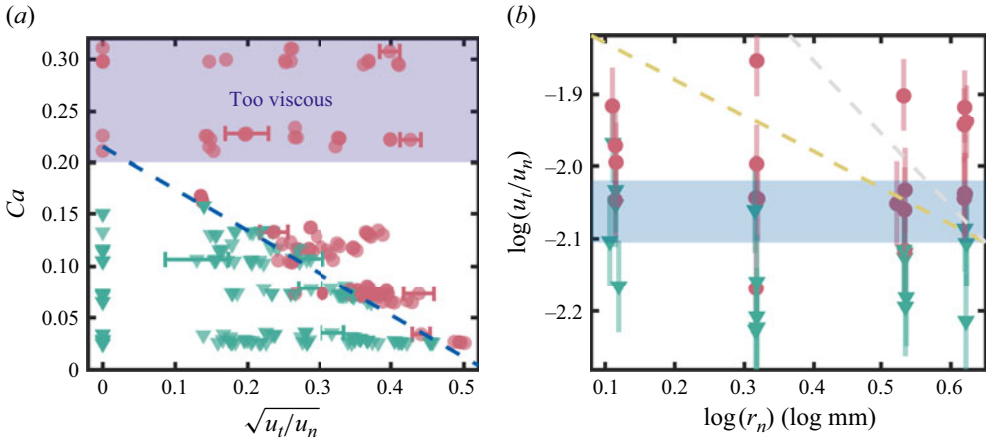

Figure 4. Upstream impact outcomes for normal droplet impact on a moving deep pool. Red circular markers indicate a lamella, while green triangular markers indicate an SES outcome. (*a*) This regime map includes all experimental conditions described in § 2.1: $We \in [134, 450]$ and $Re \in [940, 7930]$. The same regime map with markers coloured by the fluid involved is provided in the supplementary material. Selected data points (serving as representative examples) have horizontal error bars based upon a propagation of error analysis that assumes absolute errors ± 0.02 m s^{-1} for u_t and ± 0.01 m s^{-1} for u_n (see § 2.1); vertical error bars are omitted as they would be smaller than the marker in each case. The blue dashed line delineates a linear least squares fit to the transition. (*b*) Plots for $Ca = 0.072 \pm 0.002$ (21 vol% and 1 cSt fluids) with $r_n \in [1.11, 1.87]$ mm to assess the influence of length scale. Error bars are included for all points, constructed as described for (*a*). The blue patch is our best estimate for the Ca transition across all r_n plotted. For comparison, the yellow and grey dashed lines indicate $\alpha = 1/4$ and $\alpha = 1/2$ exponents, respectively, which are arbitrary examples of weak r_n dependence for demonstration purposes, i.e. $r_n^{\alpha}\sqrt{u_t/u_n}$ for fixed Ca.

the maximum free surface curvatures on the droplet and pool sides of the ejecta sheet, which are denoted as points T and B in figure 3(*d*), respectively. Therein, $\theta(t)$ was defined as the angle between the horizontal and the normal to the ejecta sheet base; careful measurements showed that θ increases as $\theta \sim \sqrt{Re} \propto u_n^{1/2}$ for a static deep pool. Building upon the relationships between θ and $\beta \approx u_t/u_n$ established in the previous paragraph, we suggest that u_t acts inversely proportionally to u_n in relation to the growth of θ upstream on a moving pool, i.e. $\theta^{-1} \sim {u_t}^{1/2} \propto \sqrt{Re_t} = \sqrt{\rho u_t D/\mu}$. This analysis suggests that pool movement constrains the growth of θ upstream, although this is practically unmeasurable from our experiments. The same conclusion can be reached mechanistically by considering that the ejecta sheet base moves with the pool whilst the ejecta sheet evolves, which for an otherwise static ejecta sheet would reduce θ as sketched in figure 3(*d*). This analysis hints at the importance of the non-dimensional quantity $\sqrt{Re_t/Re} = \sqrt{u_t/u_n}$.

Figure 4(*a*) shows a regime map of Ca against $\sqrt{u_t/u_n}$, with each data point colour and shape indicating the observed upstream impact outcome (green triangle for SES, red circle for lamella). This regime map contains all of the experimental conditions described in § 2.1, including a wide range of fluid properties (see figure S2 in the supplementary material), droplet diameters, and pool/droplet velocities. Together, Ca and $\sqrt{u_t/u_n}$ nearly perfectly separate all upstream impact outcome types, producing a sharp boundary for $Ca < 0.2$. This separation holds for water, but it should be noted that the regimes do become notably more complicated to discern at the higher Weber numbers and Reynolds numbers studied (i.e. with splashing parameters $K = We\sqrt{Re} > 2 \times 10^4$) in the irregular splashing regime (Thoraval *et al.* 2012). Note that there is no upstream transition (for all

studied pool speeds) when $Ca > 0.2$, which is expected as the impact outcome is already a lamella on a static pool (Agbaglah *et al.* 2015).

Visually, the $Ca < 0.2$ transition boundary appears linear, so it is tempting to attempt a least squares linear fit. Practically, we do this for all the data (except silicone oils) for which $Ca < 0.15$, in Ca bins of 0.01, fitting to the midpoint of the first lamella and last SES outcome (when increasing pool speed), the extent of which is commensurate with the error in determining $\sqrt{u_t/u_n}$. The result is the blue dashed line in figure 4(*a*), which defines a critical capillary number corresponding to the upstream transition, $Ca_{cr} = 0.215 - 0.4059\sqrt{u_t/u_n}$, and is in good agreement with the $Ca \approx 0.16 \pm 0.01$ silicone oil data. Most notably, the fit approximately recovers the known $Ca = 0.2$ static deep pool threshold (Agbaglah *et al.* 2015), so a single constant (representing the gradient, ≈ -0.4) delineates the upstream transition alongside Ca and $\sqrt{u_t/u_n}$. Intriguingly, neither of these two quantities contains a length scale, despite the experiments in figure 4(*a*) having $D \in [2.20, 3.75]$ mm. This observation suggests that the upstream transition is length-scale-invariant, which we now investigate.

3.3. *Length-scale invariance of the upstream transition*

To assess the involvement of the length scale in the upstream transition, we consider experiments with a fixed Ca across the full range of $D = 2r_n$ studied. We suppose that $r_n^{\alpha}\sqrt{u_t/u_n} = c$, where c is a constant, and α is an unknown exponent to be determined. Hence $\log(u_t/u_n) = -2\alpha\log(r_n) + 2\log(c)$, so -2α would be the upstream transition gradient on a graph of $\log(u_t/u_n)$ against $\log(r_n)$ for fixed Ca. Such a graph (for fixed $Ca = 0.072 \pm 0.002$, 21 vol% and 1 cSt fluids) is shown in figure 4(*b*). To minimise the effect of systematic errors on this delicate investigation, the leftmost and two rightmost columns of data were collected in the same experimental session, with the dispensing tip height fixed. Only the table speed was varied, $u_t \in [0.3, 0.4]$ m s^{-1}, to access different u_t/u_n values and dispensing tips (15, 18, 30 gauge) exchanged – with the syringe pump left running – to change r_n. The $\log(r_n) \approx 0.32$ log mm column of data (using a 23 gauge dispensing tip), which happens to have the lowest $\log(u_t/u_n)$ experiment with a lamella upstream, was collected on another day. A propagation of error analysis, assuming absolute errors ± 0.02 m s^{-1} for u_t and ± 0.01 m s^{-1} for u_n (the latter being consistent with Sykes *et al.* 2023), was used to determine the error bars.

Our best estimate of the $\log(u_t/u_n)$ extent of the upstream transition is delineated in figure 4(*b*) as a blue patch, whose lowest $\log(u_t/u_n)$ value aligns with the top of the error bar for the lowest $\log(u_t/u_n)$ data point with a lamella outcome upstream (that data point mentioned in the previous paragraph). Similarly, the highest point aligns with the bottom of the error bar for the highest $\log(u_t/u_n)$ data point with an SES outcome upstream (a data point with $\log(r_n) = 0.11$ log mm and $\log(u_t/u_n) = -1.97$). That is, the transition delineated is consistent with all data points, within their assumed experimental error. Its vertical extent is so small as to appear flat, which suggests that $\alpha = 0$. By way of comparison, the yellow and grey dashed lines delineate the expected transition for relatively weak length-scale dependences of $\alpha = 0.25$ and $\alpha = 0.50$ (these being arbitrary choices for demonstration purposes), which are both anchored at the bottom of the blue patch on the right-hand side.

This analysis confirms that a parametrisation involving the only relevant length scale in the problem (r_n) is indeed not required to separate the upstream outcomes in figure 4(*a*). Notwithstanding the possibility of a complicated nonlinear dependence that our analysis may miss, the results strongly suggest that the upstream transition is length-scale-invariant.

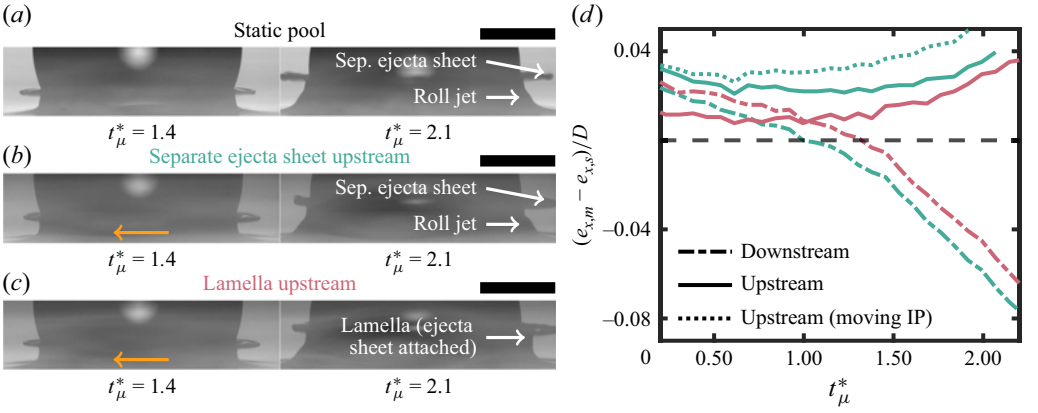

Figure 5. Geometric effects of pool rotation on ejecta sheet dynamics, at fixed capillary number. (*a–c*) High resolution (327 pixels mm^{-1}) images of the early-time ejecta sheet dynamics of $Ca = 0.115 \pm 0.004$ impact (32 vol% fluid): (*a*) static pool; (*b,c*) $u_t = 0.20 \pm 0.02$ m s^{-1}, equivalent to $\sqrt{u_t/u_n} = 0.273 \pm 0.014$, where the indicated uncertainty is derived by propagating errors. Since these parameters are close to the upstream transition (see figure 4*a*), repeated experiments can produce different outcomes: (*b*) SES upstream; (*c*) lamella upstream. Orange arrows indicate the direction of pool movement, and all scale bars are 1 mm. (*d*) Data indicating the difference between the horizontal extent of the ejecta sheet on moving and static pools, from the experiments in (*a–c*). Here, $e_{x,p}$ is the horizontal position of the ejecta sheet tip from the original impact point (IP); $p = m$ for a moving pool (either (*b*) green or (*c*) red), and $p = s$ for a static pool. In one case ('moving IP', dashed line), the IP is translated with the moving pool speed over time.

3.4. *Ejecta sheet dynamics*

To attain a detailed view of the early-time ejecta sheet dynamics, the side-view camera was replaced by a Phantom TMX 5010 (110 000 fps, 1.0 µs exposure) equipped with a Navitar 12X Zoom lens (achieving 327 pixels mm^{-1}) for the experiments in figure 5. Here, $Ca = 0.115 \pm 0.004$ (32 vol% fluid), with an SES outcome on a static pool (figure 5*a*). For both figures 5(*b*) and 5(*c*), u_t was set such that $\sqrt{u_t/u_n} = 0.27$, which is approximately the upstream transition threshold according to figure 4(*a*). Figure 5(*b*) shows an SES upstream (i.e. before the transition), whereas figure 5(*c*) has a lamella upstream (i.e. after the transition).

Qualitatively, the ejecta sheets appear similar at $t^*_\mu = 1.4$, whether the pool is static or moving. However, the vortex separation process that produces an SES outcome is known to start at $t^*_\mu = 1.05$ (Agbaglah *et al.* 2015), which must be inhibited upstream in figure 5(*c*) to generate the lamella outcome. It appears that the ejecta sheet is slightly thicker on the moving pools in figure 5, although this cannot be systematically confirmed within reasonable error tolerances with our current experimental and numerical set-ups. To do so experimentally, X-ray imaging of the ejecta sheet – such as the measurements performed by Zhang *et al.* (2012) for static deep pools – would be advisable. By $t^*_\mu = 2.1$, the impact outcomes are visually evident, and the ejecta sheet has notably different horizontal extents from the impact point $e_{x,p}$ ($p = m$ moving, $p = s$ static) upstream and downstream. These observations are confirmed quantitatively in figure 5(*d*). At approximately the aforementioned $t^*_\mu = 1.05$, the ejecta sheet considerably shortens downstream, relative to a static pool (so $e_{x,m} < e_{x,s}$), when the pool is moving (dash-dotted lines). Upstream, the ejecta sheet is always stretched (so $e_{x,m} > e_{x,s}$), even when measuring $e_{x,m}$ from the fixed impact point (solid lines). However, pool movement translates the impact point downstream, which conceivably augments ejecta sheet stretching upstream. To account

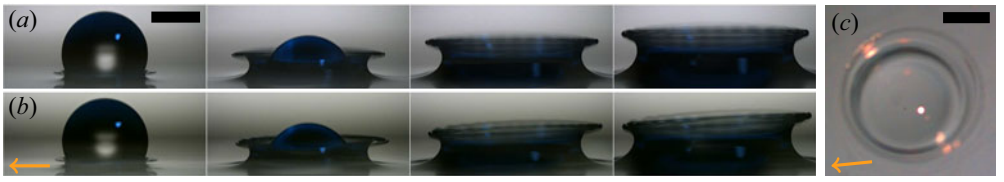

Figure 6. Typical higher viscosity impact dynamics. Images for $Ca = 0.213 \pm 0.002$ with the 43 vol% fluid: (*a*) static pool; (*b,c*) moving pool with $\sqrt{u_t/u_n} = 0.33$. The blue tinge in (*a*) and (*b*) is an artefact of repeated inner-wall surface treatments and the light source. Orange arrows indicate the direction of pool movement, and all scale bars are 1 mm.

for this effect, $e_{x,m}$ can be measured from the moving impact point (practically, adding 24 µm per t^*_μ time unit to $e_{x,m} - e_{x,s}$), which is shown in figure 5(*d*) as a dotted line for the upstream side of the figure 5(*b*) data. These analyses indicate that the ejecta sheet is considerably stretched upstream on a moving pool, which raises the prospect that pool movement thins the ejecta sheet at its base and restricts flow into it from the pool. It is this mechanism that we found to yield a lamella on sufficiently shallow pools in our previous work (Sykes *et al.* 2023), where ejecta sheet stretching was found to be caused by a pressure confinement effect of the pool base. Hence similar physical mechanisms may be at play in both configurations.

3.5. *Downstream impact outcome*

Insofar as pool movement effectively constrains the evolution of θ upstream, the opposite is true downstream. Therefore, were the root cause of the upstream transition purely geometric according to § 3.2, we might expect pool movement to recover an SES downstream when the static pool impact outcome is a lamella ($Ca > 0.2$). Throughout our experimental campaign, no such transition was seen. Figure 6 exemplifies typical dynamics for $Ca > 0.2$ on static (figure 6*a*) and relatively fast-moving (figures 6(*b,c*), $u_t = 0.29$ m s^{-1}) pools. It is notable that little asymmetry can be seen in the side views (e.g. figure 6*b*), especially at early times. Moreover, the oblique view (figure 6*c*) shows remarkably smooth dynamics and offers no hint of an instability that is typically apparent with the SES outcome.

Within the limits of the experimental design (namely limited pool speed), our results suggest that there is no lamella to SES transition downstream for $Ca > 0.2$. That is, when the pool is 'too viscous' (see the purple patch in figure 4*a*), there can be no other outcome than a lamella when the air boundary layer above the moving pool is negligible (see § 3.6). The lack of 'reversibility' in the SES–lamella transition hints at a fundamental idea relevant to both moving and static pools: the cause of the transition is not purely geometric. Rather, the association of the transition to $t^*_\mu = 1.05$ (first made by Agbaglah *et al.* 2015) suggests that the root cause of an SES outcome is an instability at the base of the ejecta sheet that enables vortex shedding. For $Ca > 0.2$, viscosity suppresses the instability and the ability to attain the SES outcome.

3.6. *Oblique impact*

The otherwise-stagnant air above a moving pool forms a boundary layer; for the steady-state rotating pool in our experiment, its characteristic thickness is $2.5\sqrt{\nu/\Omega} > 5.5$ mm (Gauthier *et al.* 2016), where ν is the kinematic viscosity of air, and $\Omega < \pi$ rad s^{-1} in this work. However, except for the presence of this boundary layer, prior to coalescence, normal droplet impact onto a moving pool is geometrically equivalent to oblique impact

on a static pool at an angle β from vertical and a velocity u_o, where $u_n = u_o \cos\beta$ and $u_t = u_o \sin\beta$. On solid surfaces, the two types of impact are equivalent regarding the resulting spreading and splashing behaviour (Buksh, Marengo & Amirfazli 2020). The boundary layer is known to have qualitative effects on impact outcomes when $u_t \gtrsim u_n$, and can even support the weight of an impacting droplet so that it 'surfs' without coalescing (Castrejón-Pita *et al.* 2016). Of course, the persistent effect of pool movement does affect longer time scale dynamics, such as bouncing, compared to an oblique impact on a static pool (Harris *et al.* 2026). However, when $u_t \ll u_n$, we hypothesise that the boundary layer does not play a decisive role on the ejecta sheet dynamics, so we would expect a transition on the leading side (equivalent to upstream on a moving pool; see § 3.2) of a sufficiently oblique impact.

Previously, oblique impacts of small droplets ($115 \pm 15\,\mu$m) have been achieved via deflection with an electric field, which is a process used in some commercial continuous inkjet printers. The resulting long time scale dynamics (e.g. crown shape and Worthington jet inclination) appear qualitatively similar to our asymmetric moving pool experiments (Gielen *et al.* 2017). However, the greater inertia of larger droplets in our study makes highly controlled oblique impacts challenging to engender experimentally, so we turn to simulations that have been used to successfully study oblique impacts previously (Cimpeanu & Papageorgiou 2018). We reproduced the experiment in figure 2(*b*) ($Ca = 0.105$, 32 vol%, $u_n = 2.45$ m s^{-1}, $u_t = 0.15$ m s^{-1}) computationally in figure 2(*c*), with good qualitative agreement. The equivalent oblique impact has $u_o = 2.455$ m s^{-1} (to three decimal places) and $\beta = 3.5°$. This very small angle is shown diagrammatically (as a green arrow) in figure 2(*d*), alongside the results of the equivalent oblique impact simulation. As predicted, a lamella is formed on the leading side rather than the SES outcome, supporting our rationale that the air boundary layer does not play a decisive role. This result suggests that our findings for moving pools are generalisable to equivalent oblique impacts, at least for the early-time dynamics of interest here.

The small value of β required to trigger an oblique impact outcome (i.e. a leading-side lamella) raises the question of whether the parabolic free surface in the radial direction of our rotating tank (i.e. out of the side-view camera focal plane – see § 2.1) is itself sufficient to induce this effect, which would affect our preceding analysis. For a fluid in solid-body rotation, the centrifugal acceleration due to rotation is balanced by the radial pressure gradient. The resulting hydrostatic balance implies a free-surface gradient

$$\frac{\mathrm{d}h}{\mathrm{d}s} = \frac{\Omega^2 s}{g}, \tag{3.1}$$

where s is the radial location from the centre of the tank (Batchelor 1967, § 4.5). Equation (3.1) is not valid near the (slightly hydrophobic) tank walls, and neglects surface tension. Not least due to the relatively narrow annulus 68 ± 1 mm used, we would expect the actual free-surface gradient at the impact point to be less than predicted by (3.1). Nevertheless, in figure 7 we plot (as solid lines) the free-surface gradient predicted by (3.1) at the upstream transition, $Ca = Ca_{cr} = f\left(\sqrt{u_t/u_n}\right)$. This fitted transition is used to obtain $\Omega = u_t/s_i$, where s_i is the radial position of the impact point, for substituting into (3.1). Here, Ω clearly depends on u_n; in figure 7, the four solid lines delineate the full extent of $u_n \in [1.6, 3.2]$ m s^{-1} for each Ca studied, which is primarily determined by the fluid used (indicated by light blue bands; see table 1). For water, the droplet impact velocity is limited to $u_n \leq 2.8$ m s^{-1}, as low-Ca fluids require a high $\sqrt{u_t/u_n}$ value for the upstream transition; for $u_n > 2.8$ m s^{-1}, the corresponding required $u_t > 0.6$ m s^{-1}

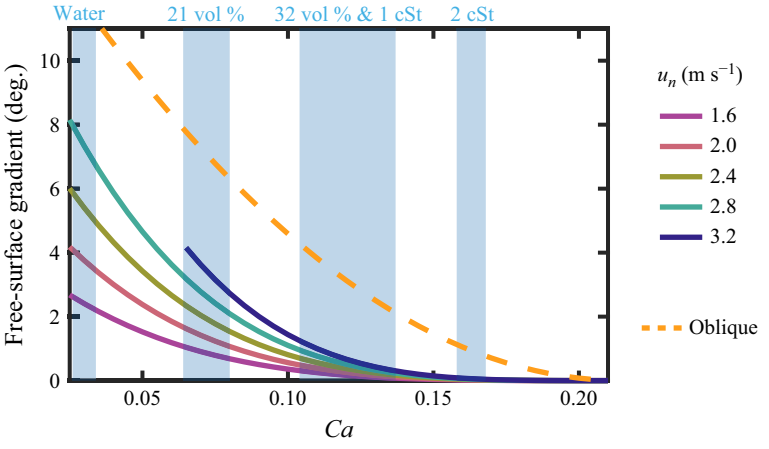

Figure 7. Due to the linear pool velocity being engendered by rotation in our work, a parabolic free surface is expected at the droplet impact point in the orthogonal direction to the linear pool movement velocity vector. Solid lines – spanning all $u_n \in [1.6, 3.2]$ m s^{-1} and $Ca \in [0.03, 0.20]$ studied (with fluids indicated in blue bands) – delineate the estimated free-surface gradient (according to (3.1)) for rotation rates corresponding to the upstream transition (which linearly varies with Ca as seen in figure 4*a*). The orange dashed line delineates the corresponding free-surface gradient expected to yield an oblique impact outcome, i.e. an uphill lamella.

becomes impractically large with our current experimental set-up. Consequently, the fitted transition for $u_n = 3.2$ m s^{-1} (dark blue line) is not shown for $Ca < 0.064$. Crucially, we would expect an out-of-plane oblique impact outcome (a lamella on the 'uphill' side of the pool here) coinciding with the upstream transition of interest when (3.1) exceeds $\beta = \tan^{-1}(u_t/u_n)$ with $Ca = Ca_{cr}$. Here, β is interpreted as the incline of the pool for a vertically impacting droplet (geometrically equivalent to the interpretation above – see § 3.2). This boundary is plotted as an orange dashed line in figure 7, which always lies well above the predicted free-surface gradient (shown by the solid lines). In addition to this analysis, the oblique camera was used to confirm pseudo-symmetric out-of-plane dynamics (i.e. no out-of-plane asymmetric outcomes) for all experiments plotted in figure 4(*a*). Hence we conclude that the parabolic nature of the free surface in our experiments is inconsequential to our results in relation to the upstream transition.

4. Conclusions

For $Ca < 0.2$ normal impacts on deep pools, the typical separate ejecta sheet (SES) dynamics transitions to a lamella only upstream, above a critical pool speed. Such asymmetric outcomes arise with little pool movement (e.g. above pool–droplet velocity ratio $u_t/u_n = 0.08$ when $Ca = 0.10$), raising the prospect that the motion of rivers and oceans may result in asymmetric dynamics following raindrop impact. The transition boundary is well-parametrised by Ca and $\sqrt{u_t/u_n}$, which are both independent of length scale. By considering experiments with fixed Ca, we concluded that the upstream transition is length-scale-invariant. We explained the importance of $\sqrt{u_t/u_n}$ physically as a constraining effect of pool movement on the ejecta sheet angle evolution upstream. A linear fit to the transition boundary recovers the known $Ca = 0.2$ threshold on static deep pools (Agbaglah *et al.* 2015). No reverse transition (lamella to SES) is seen downstream for $Ca > 0.2$, which suggests that the underlying mechanism causing the SES outcome is not purely geometric. Instead, our results suggest an instability (characterised by the visco-capillary time scale) that is suppressed by high viscosity; this conclusion applies to

any like-fluid pool impact. Our three-dimensional direct numerical simulation framework enabled us to confirm similar dynamics for an equivalent oblique impact on a static pool, suggesting that the moving pool boundary layer does not have a decisive role on impact outcomes when $u_t \ll u_n$. Our findings offer insight into common natural and industrial scenarios (e.g. ocean air–sea exchange, inkjet printing) involving moving pools where satellite droplet production is often an important consideration, as well as contributing to the fundamental understanding of the physical mechanisms that determine impact outcomes on pools more generally. Future work might extend existing studies of droplet impact onto shallow pools (e.g. Sykes *et al.* 2023), or onto pools of different miscible (e.g. Marcotte *et al.* 2019) or immiscible (e.g. Fudge, Cimpeanu & Castrejón-Pita 2021) liquids, to explore how pool movement influences ejecta sheet dynamics and splashing in contexts beyond those considered here.

Supplementary material. Supplementary material is available at https://doi.org/10.1017/jfm.2026.11586.

Acknowledgements. We thank Professor P. Read (Oxford Physics) for lending the rotating table base, D. Constable (Oxford Engineering) for helping to manufacture the annular tank, and O. Sand for setting up the rotating table at Brown. We also wish to acknowledge both reviewers, whose thoughtful comments and suggestions helped us to improve our manuscript.

Funding. This work was funded by the US National Science Foundation (NSF CBET-2123371), the UK Engineering and Physical Sciences Research Council (EP/W016036/1 and UKRI424 Core Equipment Award) and the John Fell Fund (0014320).

Declaration of interests. The authors report no conflict of interest.

Data availability. Data are available at https://github.com/OxfordFluidsLab/MovingPoolImpact, including Basilisk simulation code, underlying data tables, and videos that accompany several figures.

References

Agbaglah, G., Thoraval, M.-J., Thoroddsen, S.T., Zhang, L.V., Fezzaa, K. & Deegan, R.D. 2015 Drop impact into a deep pool: vortex shedding and jet formation. *J. Fluid Mech.* **764**, R1.

Anguelova, M.D. 2021 Big potential for tiny droplets. *Nat. Geosci.* **14** (8), 543–544.

Bao, M., Yi, Z., Zhao, D., Liu, H., Guo, Y., Gong, L. & Shen, S. 2025 Dynamic characteristics of oblique droplet impact on a liquid film. *Phys. Fluids* **37** (2), 022101.

Batchelor, G.K. 1967 *An Introduction to Fluid Dynamics*. Cambridge University Press.

Bird, J.C., Tsai, S.S.H. & Stone, H.A. 2009 Inclined to splash: triggering and inhibiting a splash with tangential velocity. *New J. Phys.* **11** (6), 063017.

Buksh, S., Marengo, M. & Amirfazli, A. 2020 Impacting of droplets on moving surface and inclined surfaces. *Atomiz. Sprays* **30** (8), 557–574.

Castrejón-Pita, A.A., Castrejón-Pita, J.R. & Hutchings, I.M. 2012 Experimental observation of von Kármán vortices during drop impact. *Phys. Rev. E* **86** (4), 045301.

Castrejón-Pita, J.R., Muñoz-Sánchez, B.N., Hutchings, I.M. & Castrejón-Pita, A.A. 2016 Droplet impact onto moving liquids. *J. Fluid Mech.* **809**, 716–725.

Cheng, N.-S. 2008 Formula for the viscosity of a glycerol–water mixture. *Ind. Engng Chem. Res.* **47** (9), 3285–3288.

Cimpeanu, R. & Papageorgiou, D.T. 2018 Three-dimensional high speed drop impact onto solid surfaces at arbitrary angles. *Intl J. Multiphase Flow* **107**, 192–207.

Crocker, J.C. & Grier, D.G. 1996 Methods of digital video microscopy for colloidal studies. *J. Colloid Interface Sci.* **179** (1), 298–310.

Fudge, B.D., Cimpeanu, R., Antkowiak, A., Castrejón-Pita, J.R. & Castrejón-Pita, A.A. 2023 Drop splashing after impact onto immiscible pools of different viscosities. *J. Colloid Interface Sci.* **641**, 585–594.

Fudge, B.D., Cimpeanu, R. & Castrejón-Pita, A.A. 2021 Dipping into a new pool: the interface dynamics of drops impacting onto a different liquid. *Phys. Rev. E* **104** (6), 065102.

Gauthier, A., Bird, J.C., Clanet, C. & Quéré, D. 2016 Aerodynamic Leidenfrost effect. *Phys. Rev. Fluids* **1** (8), 084002.

GIELEN, M.V., SLEUTEL, P., BENSCHOP, J., RIEPEN, M., VORONINA, V., VISSER, C.W., LOHSE, D., SNOEIJER, J.H., VERSLUIS, M. & GELDERBLOM, H. 2017 Oblique drop impact onto a deep liquid pool. *Phys. Rev. Fluids* **2** (8), 083602.

GREENSPAN, H.P. & HOWARD, L.N. 1963 On a time-dependent motion of a rotating fluid. *J. Fluid Mech.* **17** (3), 385–404.

GUO, W., XU, Y., WANG, J., TIAN, C., ZHAO, N. & ZHU, C. 2025 Numerical simulation of multi-angle droplet impact on flowing thin water film and secondary droplet generation. *Phys. Fluids* **37** (10), 103335.

GUPTA, G. & KUMAR, P. 2020 Splashing dynamics of a drop impact onto a deep liquid pool with moving film interface. *Phys. Fluids* **32** (1), 012102.

HAO, J. & GREEN, S.I. 2017 Splash threshold of a droplet impacting a moving substrate. *Phys. Fluids* **29** (1), 012103.

HAO, J., LU, J., LEE, L., WU, Z., HU, G. & FLORYAN, J.M. 2019 Droplet splashing on an inclined surface. *Phys. Rev. Lett.* **122** (5), 054501.

HARRIS, D.M., ALVENTOSA, L.F.L., SAND, O., SILVER, E., MOHAMMADI, A., SYKES, T.C., CASTREJÓN-PITA, A.A. & CIMPEANU, R. 2026 Bouncing to coalescence transition for droplet impact onto moving liquid pools. *J. Fluid Mech.* **1030**, A16.

HOMICZ, G.F. & GERBER, N. 1987 Numerical model for fluid spin-up from rest in a partially filled cylinder. *J. Fluids Engng* **109** (2), 194–197.

LI, D., SHANG, Y., WANG, X. & ZHANG, J. 2024 Dynamic behavior of droplet impacting on a moving surface. *Exp. Therm. Fluid Sci.* **153**, 111126.

LOHSE, D. 2022 Fundamental fluid dynamics challenges in inkjet printing. *Annu. Rev. Fluid Mech.* **54**, 349–382.

MARCOTTE, F., MICHON, G.-J., SÉON, T. & JOSSERAND, C. 2019 Ejecta, corolla, and splashes from drop impacts on viscous fluids. *Phys. Rev. Lett.* **122** (1), 014501.

POPINET, S. 2009 An accurate adaptive solver for surface-tension-driven interfacial flows. *J. Comput. Phys.* **228** (16), 5838–5866.

POPINET, S. 2015 A quadtree-adaptive multigrid solver for the Serre–Green–Naghdi equations. *J. Comput. Phys.* **302**, 336–358.

REIJERS, S.A., LIU, B., LOHSE, D. & GELDERBLOM, H. 2019 Oblique droplet impact onto a deep liquid pool. arXiv:1903.08978.

STUMPF, B., QEZELJEH, S.A., KAMAL, R., DEZITTER, F., MARTUFFO, A., ROISMAN, I.V. & HUSSONG, J. 2025 Drop impact onto a moving substrate: aerodynamic rebound. *Intl J. Multiphase Flow* **184**, 105113.

SYKES, T.C., CIMPEANU, R., FUDGE, B.D., CASTREJÓN-PITA, J.R. & CASTREJÓN-PITA, A.A. 2023 Droplet impact dynamics on shallow pools. *J. Fluid Mech.* **970**, A34.

THORAVAL, M.-J., TAKEHARA, K., ETOH, T.G., POPINET, S., RAY, P., JOSSERAND, C., ZALESKI, S. & THORODDSEN, S.T. 2012 von Kármán vortex street within an impacting drop. *Phys. Rev. Lett.* **108** (26), 264506.

THORODDSEN, S.T. 2002 The ejecta sheet generated by the impact of a drop. *J. Fluid Mech.* **451**, 373–381.

THORODDSEN, S.T., THORAVAL, M.-J., TAKEHARA, K. & ETOH, T.G. 2011 Droplet splashing by a slingshot mechanism. *Phys. Rev. Lett.* **106** (3), 034501.

WANG, H., LIU, S., BAYEUL-LAINÉ, A.-C., MURPHY, D., KATZ, J. & COUTIER-DELGOSHA, O. 2023 Analysis of high-speed drop impact onto deep liquid pool. *J. Fluid Mech.* **972**, A31.

WEISS, D.A. & YARIN, A.L. 1999 Single drop impact onto liquid films: neck distortion, jetting, tiny bubble entrainment, and crown formation. *J. Fluid Mech.* **385**, 229–254.

ZHANG, L.V., TOOLE, J., FEZZAA, K. & DEEGAN, R.D. 2012 Evolution of the ejecta sheet from the impact of a drop with a deep pool. *J. Fluid Mech.* **690**, 5–15.